Lamb-shift measurement in hydrogenic phosphorus

H.-J. Pross
Bank Verlag GmbH, 5000 Köln, Federal Republic of Germany

D. Budelsky, L. Kremer, D. Platte, and P. von Brentano
Institut für Kernphysik, Universität zu Köln, 5000 Köln 41, Federal Republic of Germany

J. Gassen
Crone GmbH, 4100 Duisburg, Federal Republic of Germany

D. Müller
Gesellschaft für Schwerionenforschung mbH, 6100 Darmstadt, Federal Republic of Germany

F. Scheuer
Target Systemelectronic GmbH, 5650 Solingen, Federal Republic of Germany

A. Pape and J. C. Sens
Centre de Recherches Nucléaires and Université Louis Pasteur, 67037 Strasbourg Cedex, France
(Received 9 June 1992; revised manuscript received 2 April 1993)

The final result of a $2s\,^2S_{1/2}$–$2p\,^2P_{1/2}$ Lamb-shift measurement by the laser resonance method in hydrogenic phosphorus is reported. Metastable $2s\,^2S_{1/2}$ ions were prepared using a $\beta \approx 0.08$ velocity beam of $^{31}P^{14+}$ ions obtained from the MP tandem accelerator at the Centre de Recherches Nucléaires in Strasbourg. From the metastable state the transition to the $2p\,^2P_{3/2}$ state was induced with a high-power dye laser leading to a measured transition energy of $\Delta E = 2.231\,33(12)$ eV. Subtracting the well-known fine-structure splitting $\Delta E_{\rm FS} = 2.314\,82(2)$ eV, the Lamb shift is deduced to be $E_{\rm expt}({\rm LS}) = 20\,188(29)$ GHz. This result is compared with the theoretical value $E_{\rm theor}({\rm LS}) = 20\,254(10)$ GHz and with other experimental results for the Lamb shift in the region $Z \leq 18$. Finally, the utility of the Lamb-shift measurements in testing the $G(Z\alpha)$ function of the self-energy, which includes only terms in $(Z\alpha)^n$, $n \geq 6$, is discussed.

PACS number(s): 12.20.Fv, 32.70.Jz, 32.30.−r, 31.30.Jv

I. INTRODUCTION

Quantum electrodynamics (QED) is an extremely successful theory leading to many predictions which have been verified by experiment. Stringent tests of its validity are, for example, those obtained from the leptonic g factor [1], the hyperfine splitting in hydrogen [2], and the radiative level shifts of simple bound systems. The Lamb shift in electronic transitions in atoms has provided one of the most fertile tests for QED. It measures predominantly the self-energy. This is in contrast to muonic systems where the vacuum polarization is dominant.

Forty-five years ago Lamb and Retherford [3] performed the first experiment measuring the $2s\,^2S_{1/2}$–$2p\,^2P_{1/2}$ level separation in hydrogen. These experiments were followed by a large number of others with decreasing errors. The recent values published by Lundeen and Pipkin [4] and Pal'chikov, Sokolov, and Yakovlev [5] have an uncertainty smaller than that of the theoretical predictions. While there is good agreement between the theoretical shift obtained using the older value of the proton radius [6] and experiment, there is some discrepancy [7] if the latest proton radius from Ref. [8] is used.

The Lamb shift can be described from QED in terms of a series expansion in α and $(Z\alpha)$. This expansion enables one to separate effects which are radiative, characterized by the fine-structure constant α, from those which have their origin in atomic binding, which are characterized by $(Z\alpha)$ [9]. In order to determine the coefficients of the higher-order terms independently, it is necessary to have accurate experimental data on the Lamb shift for several values of Z.

The main topic of this paper is a $2S$ Lamb-shift measurement in $^{31}P^{14+}$ using the $2s\,^2S_{1/2}$–$2p\,^2P_{3/2}$ laser resonance spectroscopy method by means of a flash lamp pumped high-power dye laser. In two previous papers [10,11] preliminary results of these measurements were reported. Now the final results will be presented and the experiment will be described in detail. Theoretical calculations in hydrogenlike atoms published by different authors will be reviewed in Sec. II. In Sec. III the principle of the laser resonance measurement will be summarized. Section IV contains a description of the experimental setup and the data acquisition system. The data evaluation will be described in Sec. V. The results of the $^{31}P^{14+}$ [12,13] and $^{32}S^{15+}$ measurements [14,15] will be presented and compared with other experimental values. The last section contains comments on future

perspectives of Lamb-shift measurements with the laser resonance method.

II. LAMB-SHIFT THEORY

The lowest-energy states of an electron in the Coulomb potential of a fixed point charge Ze is given by the Dirac equation. The theory predicts that the energy levels depend only on the principal quantum number n and the total angular momentum j. These eigenstates are independent of the orbital angular momentum l. Thus the $2s\,^2S_{1/2}$ and $2p\,^2P_{1/2}$ levels should be degenerate.

However, Lamb and Retherford's experiment in 1947 [3] showed that the $2s$ level is displaced upwards towards the $2p_{1/2}$ level by about 1040 MHz. This displacement indicates that the interaction between charged particles might be non-Coulombic at very short distances [16]. Introducing electric field quantization leads to radiative corrections, i.e., QED effects which remove the energy degeneracy. Because the $2s$ electron has a higher probability of staying near the nucleus where the electromagnetic field is strong, the $2s$ binding energy is raised more than the $2p$ energy. Many authors have made detailed calculations of the energy levels and the Lamb shift based on this theory.

Mohr [17] and Johnson and Soff [18] show in their calculation of the energy levels of hydrogenlike atoms that these energies are determined mainly by the Dirac equation, reduced mass corrections, and the Lamb shift. The Lamb shift is calculated as the sum of six different contributions.

The lowest order QED effect of main interest in calculating the energy levels is the *self-energy* (SE) or *vacuum fluctuation*, which includes the anomalous *magnetic moment* (AMM) of the electron. It can be calculated with Eq. (2.1):

$$\delta E_{\rm SE} = \frac{4\alpha(Z\alpha)^4 mc^2}{3\pi n^3}\left\{L_n + \frac{3}{8}\frac{C_{lj}}{(2l+1)} + \left(\ln\frac{1}{(Z\alpha)^2} + \frac{11}{24}\right)\delta_{l0} + C_{50}(Z\alpha) + (Z\alpha)^2\left[C_{61}\ln\frac{1}{(Z\alpha)^2} + C_{62}\ln^2\frac{1}{(Z\alpha)^2} + G(Z\alpha)\right]\right\}. \tag{2.1}$$

For L_n and C_{ij} see Table I. The 3/8 term contains the contribution of the magnetic moment and the terms in the large parentheses include the lowest order self-energy. The next terms are an expansion of the self-energy in powers of $(Z\alpha)$. The term $G(Z\alpha)$ includes the sixth-order remainder.

Mohr [17] calculated numerically the self-energy for $Z = 10, 20, \ldots, 60$ and Johnson and Soff [18] for $Z = 10, 20, \ldots, 110$ to all orders in $\alpha(Z\alpha)^n$ with this formula. The intermediate values are interpolated and extrapolated using a five-point Lagrangian interpolation. The finite nuclear size correction to the self-energy, taken into account only by Johnson and Soff, results in an empirical formula which follows from the exact calculation [20].

In calculating the *vacuum polarization* (VP) contribution, one starts with the Coulomb potential corrected with the Uehling potential [21], which is a correction in lowest order in α and $(Z\alpha)$. The higher order terms in $(Z\alpha)$ are calculated in [18,22]. The corrections due to finite nuclear size effects are included. In Ref. [23] a closed formula for the vacuum polarization is given:

$$\delta E_{\rm VP} = \frac{\alpha(Z\alpha)^4}{6\pi}mc^2\left[-\frac{1}{5} + \frac{5}{64}\pi(Z\alpha) - 0.0425(Z\alpha)^2 + 0.1030(Z\alpha)^3 - \frac{1}{10}(Z\alpha)^2\ln\frac{1}{(Z\alpha)^2} + (Z\alpha)^2 H(Z\alpha)\right]. \tag{2.2}$$

The numerical values in Eq. (2.2) are given to calculate the $2S$ Lamb shift. For other states, coefficients have to be applied. The function $H(Z\alpha)$ is analogous to the function $G(Z\alpha)$ in Eq. (2.1) and contains the higher-order $(Z\alpha)$ contributions to the vacuum polarization but its value is much smaller than that of $G(Z\alpha)$.

The nuclear charge distribution, or finite size of the nucleus (FSN), modifies the behavior of the Coulomb potential for *short* distances. The charge distribution is assumed to be represented by that of a homogeneously

TABLE I. Bethe logarithms L_{nl} and coefficients C and δ_{l0} for calculating $H(Z\alpha)$ with Eq. (2.1). The L_{nl} and C are taken from Refs. [18,19].

State	L_{nl}	C_{50}	C_{61}	C_{62}	δ_{l0}	C_{lj}	a_{nl}	b_{nl}
$1s\,^2S_{1/2}$	-2.984	6.968	4.065	-0.75	1	1	$124/24 + (7/2)\ln 2$	36/40
$2s\,^2S_{1/2}$	-2.811	6.968	4.448	-0.75	1	1	187/24	36/40
$2p\,^2P_{1/2}$	0.030	0	0.429	0	0	-1	-7/24	-10/40
$2p^2P_{3/2}$	0.030	0	0.242	0	0	1/2	-7/24	5/40

charged sphere of radius R. This effect studied in Ref. [24] gains in importance mainly for higher Z and affects the s states more than the p states:

$$\delta E_{\mathrm{FSN}} = \tfrac{1}{12}\ \left[1 + 1.19(Z\alpha)^2\right](Z\alpha)^2 \times \left(\frac{(Z\alpha)0.836A^{1/3}}{\lambda_C}\right)^{2s} mc^2, \qquad (2.3)$$

where $s = \sqrt{1-(Z\alpha)^2}$. A is the atomic number and λ_C is the Compton wavelength of the electron. If an experimental value for the nuclear radius is available the term $0.836A^{1/3}$ can be replaced by this value.

The *relativistic corrections* (RC), i.e. the *relativistic recoil* (RR) and the *relativistic reduced mass* (RM) corrections, result in two additional corrections of order Zm/M and m/M, respectively. These corrections have been computed to lowest order in $(Z\alpha)$. Higher-order terms have not been calculated, so the uncertainties are assumed to be equal to the lowest-order terms;

$$\delta E_{RC} = \frac{4\alpha(Z\alpha)^4}{3\pi n^3} mc^2 \frac{m}{M} \times \overbrace{\left\{ Z\left[\frac{1}{4}\ln\frac{1}{(Z\alpha)^2}\delta_{l0} + 2L_{nl} + a_{nl}\right] - \underbrace{\left[3\ln\frac{1}{(Z\alpha)^2}\delta_{l0} + 3L_{nl} + b_{nl}\right]}_{E_{RM}}\right\}}^{E_{RR}}. \qquad (2.4)$$

Up to now all radiative corrections are called lowest-order corrections as they are caused by only one virtual photon (α). The final correction considered is the radiative correction to the one-electron energies which are due to the exchange of two virtual photons (α^2). They are called *higher-order* (HO) corrections. These corrections again consist of a vacuum polarization, a self-energy, and an anomalous magnetic moment contribution and have been worked out analytically to lowest order in ($Z\alpha$). Their total is estimated as

$$\delta E_{\mathrm{HO}} = \frac{\alpha}{\pi} \times \overbrace{\left\{ \overbrace{\left(-\frac{41}{54}\right)}^{\mathrm{VP}} \overbrace{-\frac{4819}{1728} - \frac{49}{144}\pi^2 + \frac{3}{2}\pi\ln 2 - \frac{9}{4}\zeta(3)}^{\mathrm{SE}} \right)\delta_{l0} + \underbrace{\frac{C_{lj}}{2l+1}\left(\frac{197}{192} + \frac{\pi^2}{16} - \frac{3\pi^2}{8}\ln 2 + \frac{9}{16}\zeta(3)\right)}_{\mathrm{AMM}} \right\}}. \qquad (2.5)$$

For phosphorus the total Lamb shift calculated with Eqs. (2.1)–(2.5) results in the following values:

E_{LS}	=	δE_{SE}	+	δE_{VP}	+	δE_{FSN}	+	δE_{HO}	+	δE_{RC}	
100%		105.80%		−6.42%		0.57%		0.03%		0.03%	
20254(10)		21393(8)		−1260		112(1)		5(5)		6(6)	(GHz) .

(2.6)

In Ref. [25] the Källen-Sabry contribution to the Lamb shift in hydrogenlike atoms, the vacuum polarization potential of order $\alpha^2(Z\alpha)$, is evaluated. The corresponding energy shift for $Z = 15$ raises the vacuum polarization value of about 10% of the theoretical uncertainty of the Lamb shift. Because the vacuum polarization contribution has a negative sign, the total Lamb shift is reduced.

In Ref. [9] the radiative recoil contributions to the Lamb shift in the external-field approximation are described. This results in an additional contribution of order $\alpha(Z\alpha)^5 m^2/M$ beyond that expected from the reduced mass effects. The new term is

$$\Delta E = \frac{4\alpha(Z\alpha)^4 mc^2}{3\pi n^3} \times \left[(Z\alpha)\frac{m}{M}\frac{3}{4}\frac{\pi}{c^2}\left(\frac{35}{4}\ln 2 - \frac{39}{5} + \frac{31}{192}\right) - 0.415 \pm 0.004\right]. \qquad (2.7)$$

Including the correction of order $\alpha(Z\alpha)^6 m^2/M$ [26], this result reduces the theoretical Lamb shift in the hydrogen $n = 2$ state by about 3 ppm or −3.33 kHz. Extrapolating to $Z = 15$, a contribution of 80 MHz is found [27].

III. PRINCIPLE OF THE MEASUREMENT

The laser resonance measurement uses the isomeric $2s\,^2S_{1/2}$ state of the hydrogenlike atom whose lower levels are shown in Fig. 1. This state is metastable because the electric dipole transition to the $1s\,^2S_{1/2}$ ground state is forbidden by the parity selection rule $P = (-1)^l$ and by the orbital-angular-momentum selection rule $\Delta l = \pm 1$. The transition probability between the $2s\,^2S_{1/2}$ and $2p\,^2P_{1/2}$ states is diminished by the small energy difference. Thus the dominant decay channel for the $2s\,^2S_{1/2}$ state at $Z \approx 15$ is a $2E1$ transition to the ground state. The decay rates of this transition in phosphorus and sulfur are presented in Table II.

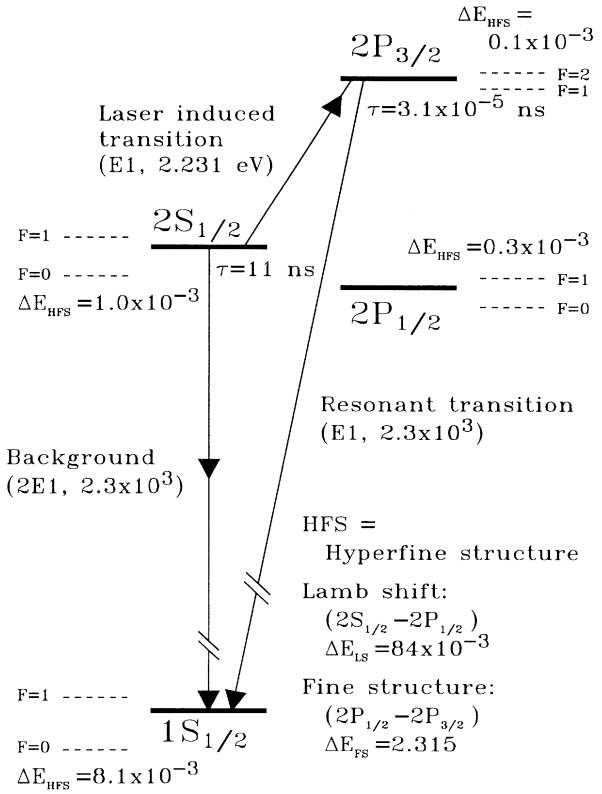

FIG. 1. Partial level scheme including the hyperfine structure for the $n \leq 2$ levels in hydrogenlike atoms (not to scale). All energies are in units of eV. The energy and lifetime values are for $^{31}P^{14+}$.

From the $2s\,^2S_{1/2}$ isomeric state a transition to the $2p\,^2P_{3/2}$ level is induced by the laser. The $2p\,^2P_{3/2}$ state decays subsequently by a fast $E1$ Lyman-α x-ray transition to the ground state. Table II presents the lifetimes and decay rates of these states.

Neglecting deviations which are small compared to the resolution of this experiment, the number N^{res} of emitted Lyman-α x rays as a function of the photon energy $E_{\mathrm{c.m.}}$ of the laser light results in a Lorentzian distribution;

$$N^{\mathrm{res}}(E_{\mathrm{c.m.}}) = N^0 \times \frac{\left(\frac{\Gamma}{2}\right)^2}{(E_{\mathrm{c.m.}} - E^0)^2 + \left(\frac{\Gamma}{2}\right)^2}. \tag{3.1}$$

The centroid energy E^0 of this function is the $2s\,^2S_{1/2}$–$2p\,^2P_{3/2}$ transition energy. Subtracting E^0 from the well-known $2P\,^2P_{1/2}$–$2p\,^2P_{3/2}$ fine-structure splitting [18] yields the Lamb shift. The parameter Γ is the FWHM of the Lorentzian distribution. N^0 is its amplitude, which is proportional to the laser intensity and to the ion-beam current. To obtain E^0, it is necessary to measure $E_{\mathrm{c.m.}}$ and N^{res} at different photon energies.

In order to obtain the energy $E_{\mathrm{c.m.}}$ of Eq. (3.1) the wavelength λ_{lab} of the laser photons in air is measured. The hydrogenlike ions in the metastable state are produced from a fast-ion beam with $\beta \equiv v/c \approx 0.08$, so $E_{\mathrm{c.m.}}$ is the Doppler shift corrected energy derived from the vacuum photon wavelength λ in the laser rest frame;

$$E_{\mathrm{c.m.}} = \frac{hc}{\lambda} \frac{1 - \beta\cos\theta}{\sqrt{1-\beta^2}}. \tag{3.2}$$

This leads to an energy shift of $(E_{\mathrm{c.m.}} - E_{\mathrm{lab}})/E_{\mathrm{c.m.}} \approx 8\%$. β is calculated by Eq. (3.3),

$$\beta = \sqrt{1 - \frac{1}{(1 + E_{\mathrm{ion}}/M_0c^2)^2}}, \tag{3.3}$$

where M_0 is the rest mass of the ion. It is necessary to determine the angle θ between the intersecting photon and ion beams and to measure the ion energy E_{ion} which depends on the magnetic field of the accelerator analyzing magnet ($\nu_{\mathrm{NMR}}, K_{\mathrm{magnet}}$) and the energy loss ($E_{\mathrm{loss}}$) of the ions in the second stripping foil (see Sec. IV A);

$$E_{\mathrm{ion}} = E_{\mathrm{ion}}(\nu_{\mathrm{NMR}}, K_{\mathrm{magnet}}, E_{\mathrm{loss}}). \tag{3.4}$$

The wavelength of the laser is determined in air but the ions are in the vacuum of the beam line. Thus an air to vacuum correction has to be applied which depends on the air pressure P and the room temperature T:

$$\lambda = \lambda_{\mathrm{lab}}[1 + \phi(\lambda_{\mathrm{lab}}, P, T)]. \tag{3.5}$$

Due to the short lifetime ($\tau \approx 1 \times 10^{-14}$ s) of the

TABLE II. Lifetimes τ and decay rates λ of the metastable $2s\,^2S_{1/2}$ state and the $2p\,^2P_{3/2}$ state for hydrogenic phosphorus and sulfur. λ^* represents the laser induced decay rate $2s\,^2S_{1/2}$–$2p\,^2P_{3/2}$ for an assumed laser energy density of 3 MW/cm^2.

	$^{31}P^{14+}$	$^{32}S^{15+}$	Units	Reference
λ^*	1.2×10^8	8.0×10^7	s^{-1}	[28]
$\lambda_{2E1}(2S_{1/2} \rightarrow 1S_{1/2})$	9.3×10^7	1.4×10^8	s^{-1}	[29]
$\lambda_{M1}(2S_{1/2} \rightarrow 1S_{1/2})$	1.5×10^6	2.8×10^6	s^{-1}	[29]
$\lambda_{E1}(2S_{1/2} \rightarrow 2P_{1/2})$	1.2×10^2	2.2×10^2	s^{-1}	[30]
$\tau_{\mathrm{tot}}(2S_{1/2})$	10.6	7.0	*ns*	
$\lambda(2P_{3/2} \rightarrow 2S_{1/2})$	4.7×10^5	9.1×10^5	s^{-1}	[31]
$\lambda(2P_{3/2} \rightarrow 1S_{1/2})$	3.2×10^{13}	4.1×10^{13}	s^{-1}	[32]
$\tau_{\mathrm{tot}}(2P_{3/2})$	3.1×10^{-5}	2.4×10^{-5}	ns	

$2p\,^2P_{3/2}$ state the induced transition has a width ($\Gamma \approx 4$ nm) large compared to the laser linewidth ($\Gamma_\lambda \approx 0.2$ nm). Because of the required wide tuning range of the laser, the wavelength dependency of the light transmitting media must be well known.

Unfortunately, it is not possible to measure the $N^{\rm res}$ in Eq. (3.1) directly. The two-photon decay $2s\,^2S_{1/2}$–$1s\,^1S_{1/2}$ leads to a significant number of background counts N^B. The total energy of this $2E1$ radiation is nearly the same (see Fig. 1) as the energy of the resonance $2p\,^2P_{3/2}$–$1s\,^1S_{1/2}$;

$$\frac{E(2P_{3/2}-1S_{1/2})-E(2S_{1/2}-1S_{1/2})}{E(2P_{3/2}-1S_{1/2})} \approx 1\times 10^{-3}. \tag{3.6}$$

Thus the measurement of resonant counts $N^{\rm res}(E_{\rm c.m.})$ needs the background subtraction given in Eq. (3.7):

$$N^{\rm res}(E_{\rm c.m.}) = N\left(E_{\rm c.m.}, t^{\rm res}\right) - N\left(t^B\right)\frac{t^{\rm res}}{t^B}. \tag{3.7}$$

$N(t)$ is the number of x-ray counts in the time interval t. The laser pulse irradiates the ion beam in the time interval $t^{\rm res}$. A second interval t^B is used to determine the background count rate.

IV. EXPERIMENTAL SETUP

A schematic view of the experimental setup of the Lamb-shift measurement on phosphorus is shown in Fig. 2. The MP tandem accelerator at the Centre de Recherches Nucléaires in Strasbourg generated a beam of phosphorus ions with different charge states and different energies. Because the relative intensity of the P^{8+} ions was the largest ($I_{\rm ion} \approx 0.6\,\mu A$), these ions with a fixed energy of about 100 MeV were selected with the 90° analyzing magnet (AM). A thin carbon foil ($70\,\mu g/cm^2$) in the beam line was used to strip more electrons from the ions. A second magnet (CsM) together with a $\varnothing = 0.9$ mm collimator selected the hydrogenlike ions. This beam foil technique is described in more detail in Ref. [33]. About 1% of the one-electron ions are in the $2s\,^2S_{1/2}$ isomeric state (Fig. 1) which is the beam species used for the laser resonance experiment.

The photon beam from a flash lamp pumped high-power dye laser [34] intersected the ion beam at an angle $\theta = 176°$ to induce the $2s\,^2S_{1/2}$–$2p\,^2P_{3/2}$ transition. Around the intersection volume two proportional counters were mounted to monitor the emitted Lyman-α x rays. These proportional counters were also used to measure the intensity of the isomeric beam by counting the background x rays. The detected signals were prepared by fast timing electronics (El), analog-to-digital converted, counted, and stored in a computer (HP).

After the laser light had traversed the intersection volume, the beam was reflected into a monochromator (MC1), a pulse energy meter (EM), a CCD spectrometer (MC2), and a fast photodiode (PD) to measure the various laser parameters. These data were also stored for off-line evaluation.

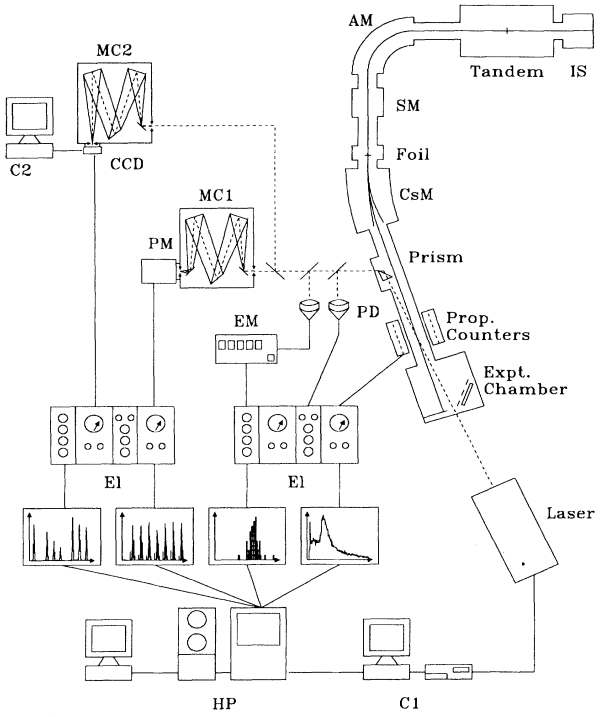

FIG. 2. Experimental setup of the laser resonance experiment (not to scale). IS: Ion source; AM: 90° analyzing magnet; SM: Switching magnet; CsM: Magnet to select the hydrogen-like ions; PD: Photodiode; EM: Energy meter; PM: Photomultiplier; CCD: CCD camera; El: Electronics; HP: Main computer; C1: Laser computer; C2: CCD computer; MC1 and MC2: Monochromator (1) and (2).

The following data were analyzed separately: Ion beam energy (Sec. IV A), laser wavelength (Sec. IV B), angle between laser and ion beam (Sec. IV C), laser energy (Sec. IV D), x-ray data (Sec. IV E).

A. Ion beam energy

The energy $E_{\rm ion}$ of the $^{31}P^{8+}$ ions was determined during normal operation by a NMR probe in the gap of the accelerator analyzing magnet. A plot of the NMR frequency $\nu_{\rm NMR}$ versus time is shown in Fig. 3.

The frequency of the NMR probe is proportional to the magnetic field. The proportionality constant $K_{\rm magnet}$ was determined with a nuclear resonance measurement.

The $^{31}P^{8+}$ ions lose about 1% of their energy in the carbon stripper foil needed for the preparation of the $^{31}P^{14+}$ hydrogenic ions. Because the energy loss $E_{\rm loss}$ depends on the stripper foil thickness and the foil thickness depends on beam irradiation time, $E_{\rm loss}$ was measured at regular time intervals.

1. Accelerator calibration

The determination of the magnet constant $K_{\rm magnet}$ of the analyzing magnet was made by measuring pro-

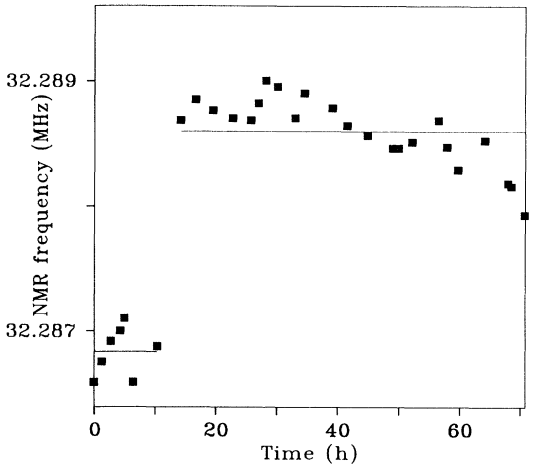

FIG. 3. NMR frequency of the accelerator analyzing magnet vs time. The data were split into two regions where different energy values are fitted. The data in the gap were not used for evaluation.

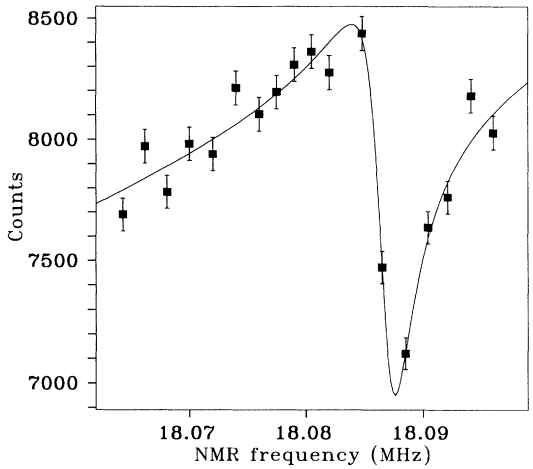

FIG. 4. Number of counts at the $^{12}C(p,p_0)^{12}C$ resonance at 14.230 75(20) MeV vs the NMR frequency of the beam analyzing magnet. The error bars denote only the statistical error.

ton elastic scattering from $T = \frac{1}{2}$ and $T = \frac{3}{2}$ resonances of carbon nuclei. The corresponding reactions are $^{12}C(p,p_0)^{12}C$ with the energies E_i and total widths Γ_i;

$$E_1 = 13.13(2)\ \text{MeV}, \quad \Gamma_1 \cong 180\ \text{keV}\ [35],$$

$$E_2 = 14.23075(20)\ \text{MeV}, \quad \Gamma_2 \leq 2\ \text{keV}\ [36,37].$$

The width of the first resonance is too large to be useful for an accurate calibration but it is helpful in finding the position of the narrow resonance. By tuning the magnetic field in one direction only from lower to higher field strength to avoid hysteresis changes, the NMR frequency and therefore the nuclear reaction resonance curve was scanned and the intensity of the scattered protons at each frequency was measured. The peak intensity of the scattered protons normalized to the ion-beam current is proportional to the differential cross section. The number of counts vs the NMR frequency for the narrow $T = \frac{3}{2}$ resonance is shown in Fig. 4. The NMR resonance frequency ν_0 and the total width Γ were obtained from Eq. (4.1):

$$N = N_0 + P(\nu - \nu_0) + \frac{Q(\nu - \nu_0) + \frac{1}{4}R\Gamma^2}{(\nu - \nu_0)^2 + \frac{1}{4}\Gamma^2}. \qquad (4.1)$$

The values P, Q, and R are additional fit parameters. With this equation the calibration constant K_{magnet} was calculated to be [38]:

$$K_{\text{magnet}} = \frac{M_0}{q^2\nu_{\text{NMR}}^2} E_{\text{ion}} \left[1 + \frac{E_{\text{ion}}}{2M_0c^2}\right]. \qquad (4.2)$$

Here E_{ion} denotes the kinetic energy, M_0 the rest mass, and q the charge state of the accelerated ions. ν_{NMR} is the measured NMR frequency. The value obtained was

$$K_{\text{magnet}} = 44.1528(35)\ \frac{\text{keV amu}}{(\text{MHz})^2}.$$

Tuning the magnetic field can lead to a small variation of the beam geometry that could affect the counting rate by less than 5%. The small energy loss of the protons in the carbon target is included in the above value. The uncertainty of the proton mass has a negligible effect on K_{magnet}.

The calibration constant K_{magnet} was determined at the magnetic field of $B \cong 4$ kG. For preparing the hydrogenlike ions a magnetic field of $B \cong 7$ kG is necessary and an estimation of the change in K_{magnet} has to be made. This correction of about $\Delta B/B = 5 \times 10^{-4}$ and an error of equal size was given in [38,39].

2. *Energy loss*

In the beam line a thin carbon foil (Foil in Fig. 2) was installed to prepare the hydrogenlike ions. Downstream (Fig. 5) from this foil a gold target (GT) and a semiconductor particle detector (PD) were installed to measure the energy loss of the ions in the stripping foil. By detecting scattered protons after a two-hole diaphragm in front of the detector it is possible to obtain the energy loss of the ions in the stripper foil. With Rutherford's formula one gets the ion energy at the two scattering angles θ_i,

$$E(\theta_i) = E_0 \frac{M_P^2}{(M_P + M_{Au})^2} \times \left[\cos\theta_i + \sqrt{\left(\frac{M_{Au}}{M_P}\right)^2 - \sin^2\theta_i}\right]^2, \qquad (4.3)$$

where M_P and M_{Au} are the masses of ^{31}P and ^{197}Au. E_0 is the energy of the incoming ions and θ_i are the scattering angles corresponding to the two holes. These angles were chosen to produce an energy difference similar to the energy loss in the stripper foil, in order to min-

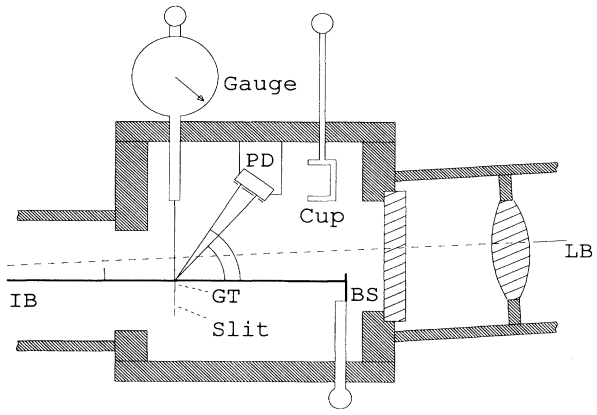

FIG. 5. Schematic diagram of the experimental chamber. PD: Particle detector; IB: Ion beam; LB: Laser beam; GT: Gold target; BS: Beam stop.

imize the uncertainty of the zero energy point and the nonlinearity over the energy range. The calibration of the detector was taken to be linear in the energy region $|E(\theta_1) - E(\theta_2)| \leq 1.5$ MeV depicted in Fig. 6.

The silicon surface barrier detector used was found [28] to give very nearly the same energy response at different points on its surface. The detector could be moved behind a collimator so that different parts of the sensitive area were reached by the scattered particles. The deviation of the peak centroids for different detector positions was less than 2×10^{-4}, which is 0.016 MeV for a 100 MeV P beam.

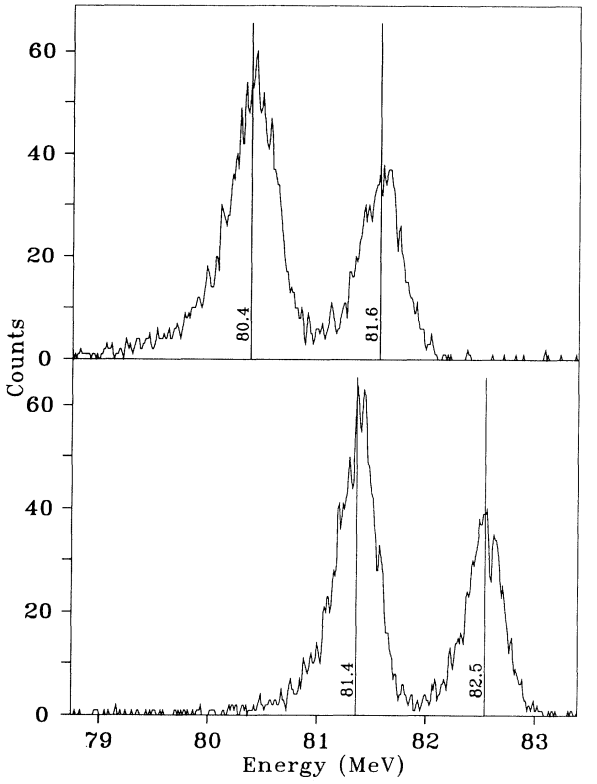

FIG. 6. Energy spectra of the semiconductor particle detector (PD in Fig. 5) with (top) and without (bottom) carbon stripping foil. One can see an energy loss of $E_{\text{loss}} \approx 1.0$ MeV which is very similar to the energy difference $E_{\text{dif}} \approx 1.1$ MeV caused by the two holes.

B. Wavelength measurement

1. Monochromator

Behind the intersection volume the laser light was reflected by a prism (see Fig. 2) out of the ion-beam line. After its intensity was decreased by a factor of 10^8, the laser beam reached a modified McPherson EU 700 [40] grating monochromator. The accuracy of the wavelength determination was increased by a factor of 2 by working in the second order of the 1180 lines/mm grating.

The shaft which turns the grating was connected to a precision potentiometer so that the position of the grating was available as an electrical signal. This signal and the output of the detecting photomultiplier were processed by electronics to give a spectrum format more usual for analyzer systems. To get one wavelength spectrum of the laser light it was necessary to measure about 35 pulses turning the monochromator grating after each pulse.

2. CCD spectrometer

To determine the wavelength λ_{lab} of single laser pulses a special wavelength spectrometer [41] has been developed (Fig. 7). The optical part is based on the same McPherson monochromator [40] but with the second 90° mirror removed. In the exit focal plane a one-dimensional CCD array, type Fairchild 133 [42], with 1024 light sensitive elements was mounted. The normal monochromator grating has been replaced by a special echelette grating

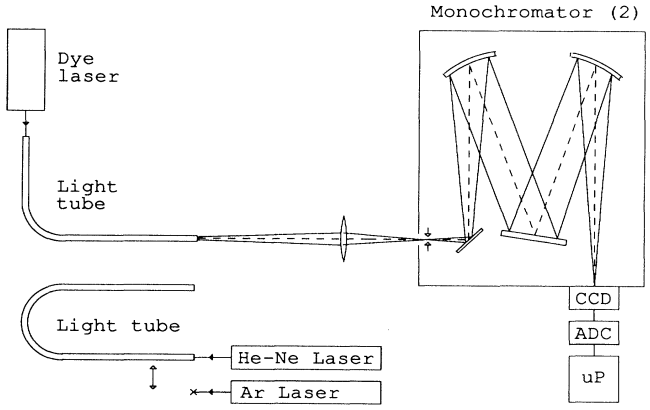

FIG. 7. Setup of the CCD spectrometer. CCD: CCD line camera; ADC: Analog to digital converter; uP: Microprocessor.

with 43.57 lines/mm, Blaze angle 59°, working in a high diffraction order. The linear dispersion of 0.84 nm/mm for the 60th order was selected. In combination with the CCD whose single element width is 13 μm, a resolution of 0.011 nm/channel could be reached. The analog signals produced by the CCD chip were processed by fast electronics, then analog-to-digital converted (A-D) and computer analyzed.

The laser output was displayed in the 61st or 62nd order depending on the wavelength. It was possible to display a He-Ne laser line in the 58th and 59th order at the same time to have a relative calibration during the measurement.

Before and after the Lamb-shift measurements this spectrometer was calibrated with eight spectral lines of an argon-ion laser. Three of these lines are displayed in two orders in Fig. 8. For each wavelength many spectra were measured and evaluated individually. Figure 8 shows the sum of all individual spectra which were used for calibration.

C. Angle between the laser and the ion beam

To transform the energy of the laser photons from the laboratory system to the rest frame of the ions the Doppler shift correction given in Eq. (3.2) has to be used. To determine the Doppler shift, the angle θ between the laser and the ion beam has to be measured accurately. This was done with a gauge mounted slit which scans the two beams separately (Fig. 5). The laser intensity behind the slit was measured with the energy meter to be described in Sec. IV D. For each $\Delta x_{\rm las} = 0.25$ mm step the intensity was averaged over ten pulses. This was done three times during one beam time period. The ion beam current was scanned with steps of $\Delta x_{\rm ion} = 0.20$ mm and its intensity was measured with a Faraday cup. Examples of intensity profiles are shown in Fig. 9. Knowing the distance of this slit from the beam intersection point, one calculates the angle between the laser and the ion beam to be $\theta = 175.78(5)°$.

D. Laser energy

The energy P of all single laser pulses was determined with the laser-pulse energy meter Polytec Rj-7000 [43] which uses the pyroelectrical principle. The laser pulse energy is completely absorbed in the probe which is heated up. The temperature dependent electrical polarization causes a change of the potential over the detector which is processed by a preamplifier and an analog-to-digital converter. An integrated microcomputer converts the data and transfers then to the main computer. The data are stored in a spectrum format where the channel number corresponds to the laser-pulse energy P and the ordinate to the number of events with a given energy. Such a spectrum is shown in Fig. 10. This equipment measures the laser-pulse energy with an absolute accuracy of about 1%. The relative accuracy is better than $\Delta P/P \leq 5 \times 10^{-3}$. Because the laser energy is used for normalization, only the relative accuracy is relevant.

E. X-ray detection

The x rays ($E_{\rm x\ ray} \approx 2.3$ keV) caused by the $2s\,^2S_{1/2}$–$1s\,^1S_{1/2}$ background decay or by the spontaneous $2p\,^2P_{3/2}$–$1s\,^1S_{1/2}$ decay were monitored by two proportional counters [44]. To get the best quantum efficiency they are filled with an argon-methane (90–10 %) mixture flowing at a pressure of 25 hPa above atmospheric. The proportional counters were separated from the vacuum of the beam line by a 6 μm thin grid supported Hostaphan

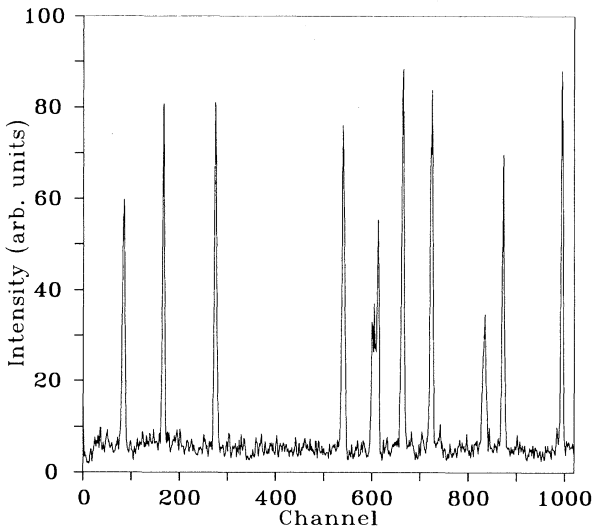

FIG. 8. Sum spectrum of argon-ion laser for calibration of the CCD spectrometer.

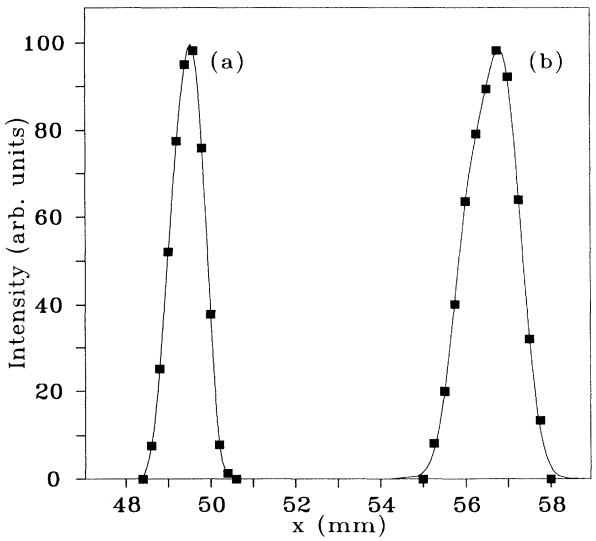

FIG. 9. Scans of (a) the ion-beam profile and (b) the laser beam profile.

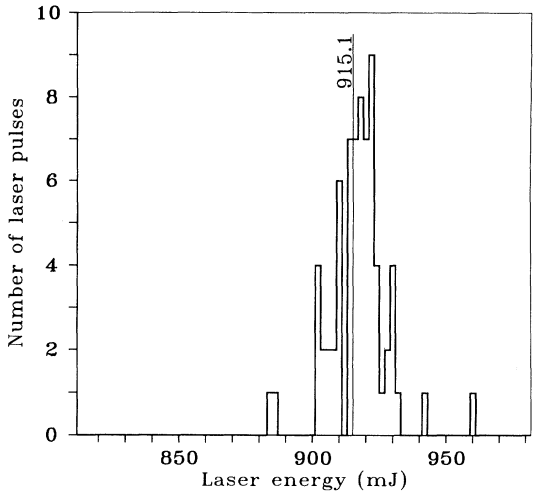

FIG. 10. Energy spectrum of 70 laser pulses at one wavelength position (PO).

foil [44] upon which an aluminum film had been evaporated. The aluminum layer was necessary in order to have a symmetrical electric field inside the proportional counters and to prevent scattered laser light from entering the counters. The energy resolution obtained with a test source (^{55}Fe, $E_\gamma = 5.9$ keV) was about 30%. Thus it was not possible to distinguish between the resonance emission and the background x rays.

The two detectors were mounted above and below the beam line because the linear polarization of the laser light causes a preferential emission of the resonant x rays in these directions. By properly choosing the proportional counter foils a peak to background ratio of 4 was reached in these measurements.

The signals produced by the proportional counters (PC) were processed by a fast preamplifier (Fig. 11) forming signals with a rise time of $\tau_r = 0.1\,\mu$s and a decay time of $\tau_f = 50\,\mu$s. The gas amplification, related to the high voltage between the anode and cathode, was adjusted so that it was possible to detect about five simultaneous resonant x rays before reaching signal saturation. These signals were differentiated in a timing filter amplifier. A constant fraction discriminator generated separated logical pulses if the x rays were separated by a time interval of at least $\tau = 80$ ns. If two x rays arose with a smaller delay they were detected as one pulse. The total probability for the detection of an absorbed photon was $\geq 97\%$ in the middle of the resonance and larger at the sides. These logical pulses were monitored in four different counters, i.e., two for each detector. During the first time interval the events $N(t^{\rm res})$ and during the second the events $N(t^B)$ were registered. The laser beam was detected by a photodiode (PD) which furnished a fast logical pulse to activate the electronics of the proportional counters. This signal was also used as a start signal for two time-to-amplitude converters (TAC). The first count of each detector stopped the corresponding TAC. The resulting time spectrum will indicate any electrical disturbances from the laser.

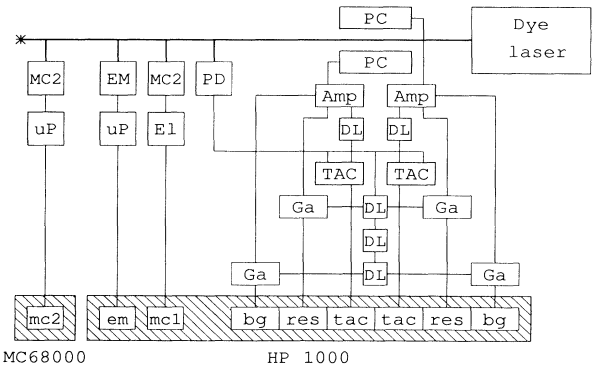

FIG. 11. Electronic setup. PC: Proportional counter; Amp: Preamplifier, timing filter amplifier, and constant fraction discriminator; DL: Delay line; TAC: Time to amplitude converter; Ga: Gate; PD: Photodiode; MC: Monochromator; El: Monochromator electronics; EM: Energy meter; uP: Microprocessor. Lowercase abbreviations denote the contributing spectrum.

F. Organization of the measurement and data

One full scan of the resonance curve [Eq. (3.1)] in cycle n consisted of measuring the $2s\,^2S_{1/2}$–$2p\,^2P_{3/2}$ transition probability at seven wavelengths λ_{in}. At each of these seven points 70 laser pulses were registered, so that one cycle had 490 laser pulses. During one beam time period more than $n = 150$ of these cycles could be measured. In Table III the organization of the measurements is summarized.

The following data were registered for each measuring point i in cycle n: The wavelength of the laser λ_{in}, the number of counts $N_{in} = N_{in}(t^{\rm res})$ in the time interval $t^{\rm res} = 7\,\mu$s in which the laser pulse irradiated the beam, the number of background events $N_{in}^B = N_{in}(t^B)$ in the time interval $t^B = 7000\,\mu$s, which started $50\,\mu$s after the laser pulse, and the laser-pulse energy P_{in}.

TABLE III. Organization of the measurement. PO: position, CY: cycle.

Number of laser pulses		Measured value, action
	1	Wavelength, pulse energy One event in each time spectrum Resonant and background events
1 PO	$\widehat{=}$ 70	Change the wavelength
7 PO $\widehat{=}$ 1 CY	$\widehat{=}$ 490	Store all data of one cycle
15 CY	$\widehat{=}$ 7500	Replace dye, adjust NMR frequency Calibration of wavelength system
30 CY	$\widehat{=}$ 15000	Replace flash lamp Check ion-beam focus
60 CY	$\widehat{=}$ 30000	Check energy loss, time windows
100 CY	$\widehat{=}$ 50000	Check laser-ion beam angle
200 CY	$\widehat{=}$ 100000	Check scattering geometry for energy loss
400 CY	$\widehat{=}$ 200000	Calibration of beam analyzing magnet

G. Control

The entire Lamb-shift experiment was controlled by several computers and electronic systems. The four counters of the x-ray detectors were read out from a HP1000 computer with an MC68000 coprocessor. This computer was the main computer used for the measurement. The two TAC spectra were also assembled in this system as were the wavelength spectra produced by the monochromator system. The energy information of the laser pulses was transformed by an MC8748 computer to a format compatible for storage of the data as spectra. All these data were recorded on magnetic tape. The wavelength information produced by the CCD spectrometer was prepared by an MC6809 for a second MC68000 system with mass storage. The organization of the overall experiment was controlled by the laser microprocessor MC8085. This computer tuned the wavelength of the laser by turning an étalon in the resonator. The grating of the monochromator wavelength system was also controlled by this system. A trigger pulse was generated to start the laser and to synchronize the CCD microcomputer system. The HP1000 computer got the information about the selected wavelength which was necessary to synchronize all assembled data. The spectra of the energy loss measurement were also fed to the HP1000 computer and were then stored on magnetic tape.

H. Dye laser

The laser used was developed especially by our group [34]. Tunability over a minimum range of 6 nm and a width of less than $\Gamma_\lambda = 0.2$ nm at a wavelength around $\lambda \approx 600$ nm was needed. The energy density was to be 10 MW/cm^2 in a focus of 1 mm^2. It is convenient to have a pulse length of several microseconds. All these requirements could be fulfilled by a flash lamp pumped dye laser. The technical details of this laser have been described in Ref. [34]. The main features are summarized in Table IV.

Due to the fast discharge of 400 J of electrical energy in the laser flash lamp, a high amount of electromagnetic noise is generated. To reduce the effects of this noise the laser system including power supply was mounted inside a double Faraday cage.

TABLE IV. Characteristics of the flash lamp pumped dye laser.

Dye	Rhodamine 6G
Solvent	Water, ammonyx LO
	N,N-dimethyldodecyl-amine-N-oxide
Pulse energy (max.)	1.2 J
Repetition rate	2 s^{-1}
Average energy	2.4 W
Total pulse length	6 μs
Tuning range	590–620 nm
Optical pumping	Quartz flash lamp in crowbar mode

V. DATA ANALYSIS

The data recorded in three different beam time periods were evaluated. When not indicated otherwise, all data discussed in the following section were taken in the last run only. There were no significant differences in the instrumentation of the previous runs except that the CCD system was used only in the last beam period.

A. Wavelength determination

In Fig. 12 the summed spectrum of the 490-laser-pulse spectra over a full scan of the resonance curve is plotted. Altogether nearly 50 000 laser-pulse spectra were detected and evaluated individually. The uncertainties of the laser wavelength determination can be classified into four groups, namely, the following:

(1) Calibration: As described in Sec. IV B 2 11 lines were used for spectrometer calibration. These energies with their associated errors were fitted with a fourth-order polynomial to give the wavelength calibration curve.

(2) Measurement: Before, during, and after the Lamb-shift beam time period He-Ne calibration spectra were recorded. These spectra were used to correct for any possible deviations caused by the transportation of the spectrometer. The shift in the peak positions results in a wavelength uncertainty.

(3) Spectrometer: In particular the uncertainties caused by the special properties of the CCD line camera (e.g., spectral response) and associated electronics (e.g., amplifier drift).

(4) Corrections: The laser beam reaches the spectrometer through a light tube of length $l \approx 80$ m. Thus the wavelength dependency of the transmission has to

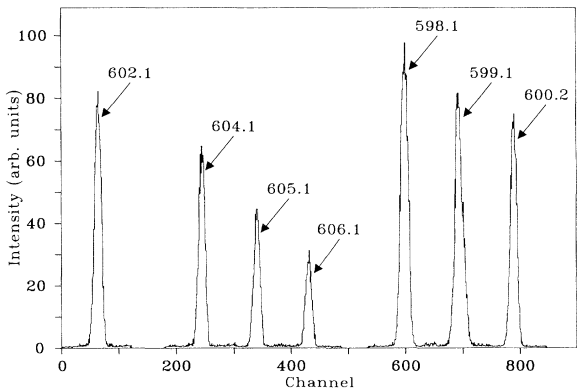

FIG. 12. Sum spectrum of 490 laser pulses of one measurement cycle (CY) over the resonance. The different intensities of the wavelength peaks are not caused by the dye laser but by the wavelength dependent transmission of the light tube used. Because wavelengths with $\lambda > 601$ nm were obtained in the 61st instead of the 62nd order of the grating, they are displayed at lower channel numbers.

TABLE V. Uncertainties of the wavelength determination with the CCD spectrometer. ΔE is the contribution to the Lamb-shift error.

Source of error	Wavelength (nm)	Relative	ΔE (meV)
Wavelength calibration	0.0052	8.7×10^{-6}	0.019
Fit	0.0036	6.0×10^{-6}	0.013
Σ	0.0063	1.1×10^{-5}	0.023
Relative calibration	0.0056	9.3×10^{-6}	0.021
CCD linearity	0.0009	1.5×10^{-6}	0.003
Pixel responsibility	0.0012	2.0×10^{-6}	0.004
Pixel width	0.0001	1.7×10^{-7}	< 0.001
Electron statistics	0.0001	1.7×10^{-7}	< 0.001
Systematic background	0.0006	1.0×10^{-6}	0.002
Digital noise	0.0032	5.3×10^{-6}	0.012
Linearity A-D conversion	0.0002	3.1×10^{-7}	0.001
Σ	0.0036	6.0×10^{-6}	0.013
Vacuum to air correction	0.0059	9.8×10^{-6}	0.022
Light tube transmission	0.0006	1.0×10^{-6}	0.002
Uncertainty of mean value	0.0030	5.0×10^{-6}	0.011
Σ	0.0066	1.5×10^{-5}	0.025
Total Σ	0.0113	1.9×10^{-5}	0.042

be taken into consideration. The wavelength is determined in air, but the ions are in the vacuum so that this correction [Eq. (3.5)] of about 0.16 nm [45] causes an uncertainty [46]. All data are stored in groups of 70 laser pulses from which follows an uncertainty caused by averaging the wavelength.

Table V enumerates the different uncertainties entering into the wavelength determination. The column Relative is normalized to the wavelength $\lambda = 600$ nm. It should be noticed that the spectrometer allows a wavelength determination with a relative accuracy of $\Delta\lambda/\lambda = 1.5 \times 10^{-5}$ [41].

B. Doppler shift

In Fig. 3 where the NMR data of the last run are plotted one can see a sudden jump in the NMR frequency 12 hours after the beginning of the measurement. For very accurate measurements it is not possible to treat the ion-beam energy as being constant so the data were split into two regions for which different ion-beam energy constants were fitted. Lamb-shift data taken during the jump were not retained. The uncertainty caused by the mean variation of the NMR frequency amounts to $\Delta\nu_{\mathrm{NMR}} = 0.0003$ MHz. This value can be converted to the errors $\Delta E_{\mathrm{ion}} = 0.002$ MeV or $\Delta E_{\mathrm{LS}} = 0.002$ MeV.

The calibration constant K_{magnet} of the 90° analyzing magnet was determined to be $K_{\mathrm{magnet}} = 44.1528(35)$ keV amu/MHz^2 which corresponds to a relative accuracy of $\Delta K/K = 7.9 \times 10^{-5}$. The extrapolation of this calibration from $B \approx 4$ to 7 kG leads to an estimated additional uncertainty of $\Delta B/B \cong 5 \times 10^{-4}$ [39,38]. Figure 13 shows the energy loss versus time for phosphorus ions in two carbon stripper foils. Foil (a) was used for the Lamb-shift measurement and foil (b) was a reference foil. Both foils show the same tendency to produce larger energy loss with increasing exposition time. The reason is a deposition of residues from the beam line onto the foils. The error bars denoted in Fig. 13 were obtained from the statistical uncertainty of the energy of the detected particles and the uncertainty of the determination of the scattering angles. Other errors not included in the figure are caused by possible inhomogeneity of the surface barrier detector and fluctuations of the counter electronics. A more detailed description of these sources of error is described in Ref. [28]. The small correction for the energy loss of the ions in the gold scattering target produces a negligible error. Table VI summarizes the various uncertainties in the determination of the ion beam energy.

The second parameter important for the Doppler shift

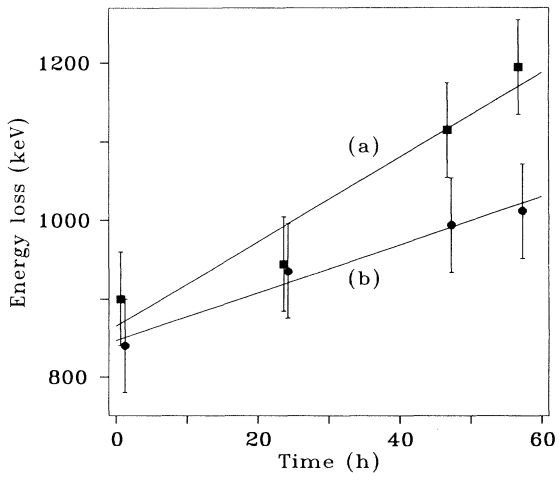

FIG. 13. Energy loss for two foils vs time. Foil (a) was used for the Lamb-shift measurement and foil (b) was a reference foil. The error bars represent only the statistical and angular uncertainty.

TABLE VI. Uncertainties in ion-beam energy determination, energy loss, and Doppler shift correction. ΔE_{ion} is the uncertainty applied to the ion-beam energy and ΔE is the contribution to the Lamb-shift uncertainty.

Source of error	Primary	Relative	ΔE_{ion} (MeV)	ΔE (meV)
	Primary energy			
Calibration 90° magnet	$0.0035\left(\frac{\text{keVamu}}{\text{MHz}^2}\right)$	7.9×10^{-5}	0.007	0.007
Extrapolation to working field		2.5×10^{-4}	0.047	0.045
Slit 90° magnet		2.0×10^{-4}	0.019	0.018
Drift 90° magnet	0.0003 (MHz)	9.3×10^{-6}	0.002	0.002
	Energy loss			
Geometry		1.7×10^{-2}	0.018	0.017
Ion-beam energy	0.049 (MeV)	5.2×10^{-4}	0.001	0.001
Inhomogeneity		2.0×10^{-4}	0.019	0.018
Statistics		3.4×10^{-2}	0.035	0.034
	Doppler shift:			
Ion-beam energy	0.049 (MeV)	5.2×10^{-4}		0.012
Energy loss	0.042 (MeV)	4.4×10^{-4}		0.039
Angle laser-ion beam	0.05 (deg)	4.0×10^{-4}		0.011

[Eq. (3.2)] is the angle between the laser and the ion beam. In order to evaluate it, the vertical position of the laser and the ion beam was measured with the gauge mounted slit (Fig. 5) in the experimental chamber. The position of the center of the ion beam could be determined with an error of $\Delta x_{\text{ion}} = 0.06$ mm and the laser beam center with $\Delta x_{\text{las}} = 0.09$ mm. The angle could thus be calculated with an accuracy of $\Delta\theta'/\theta' = 1.6 \times 10^{-2}$. This measurement has been done three times during one beam time period with a good reproducibility. To get the Doppler-corrected ion-beam energy one needs the complementary angle $\theta = 180° - \theta'$. This angle is known with a relative accuracy of 4.0×10^{-4}. Table VI contains all errors which affect the Doppler shift correction.

C. Number of resonant and background counts

The proportional counters described in Sec. IV E detect the resonant and the background x rays. The logical pulses of the proportional counters are gated with three delay generators (Fig. 11). The first delay for the detection of the resonant counts has a length of $t^{\text{res}} = 7\,\mu$s. Within this time the resonant and background events are summed. $50\,\mu$s later, a time window $t^B = 7000\,\mu$s for the detection of the background events is opened. In the last beam time period the total number of events detected in the background window amounted to $N(t^B) = 8.4137 \times 10^7$ and in the resonant time window to $N(t^{\text{res}}) = 1.436 \times 10^5$.

To obtain the true number of resonant counts one needs to know the ratio of the length of the two time windows t^{res}/t^B. This ratio was measured by counting the x rays of a radioactive source. The delays are triggered by an external pulser. The ratio of the counting rates corresponding to the ratio of the time windows could be determined with an accuracy of $\Delta(t^{\text{res}}/t^B) = 8.0 \times 10^{-3}$ (Table VII). This measurement was repeated several times during a Lamb-shift beam time period. Using this ratio, the number of resonant counts N^{res} for every laser wavelength was calculated according to Eq. (3.7) in Sec. III.

D. Time spectra

A small percentage of the laser light was reflected into a subnanosecond photodiode [47] to generate a fast time signal. This signal was used to synchronize the gates of the proportional counter electronics with the laser light and to start a TAC. The TAC was stopped by the first event registered by the proportional counters. Because only one x ray per laser pulse was registered in these spectra they could not be used for determining the Lamb shift. Two summed time spectra are shown in Fig. 14. Spectrum (a) in this figure is a normal *clean* time spectrum without high frequency disturbances produced by the laser. Because these electric disturbances were produced by the strong discharge of the capacitor through the flash lamp, they occur within 2 μs before the light emission. By discriminating the proportional counter signals one can eliminate these disturbances. In spectrum (b) one can clearly see the narrow peak at about 1.2 μs produced by the hf disturbance. This occurred at irregular time intervals caused by the wear of the spark gap of the laser. The electrical disturbances can be removed

TABLE VII. Statistical uncertainties related to the x-ray detection.

Source of error	Relative	ΔE (meV)
N (7000 μs)	1.1×10^{-4}	0.004
N (7 μs)	2.8×10^{-3}	0.090
Resonant counts	2.8×10^{-3}	0.090
Time windows	8.0×10^{-3}	0.001

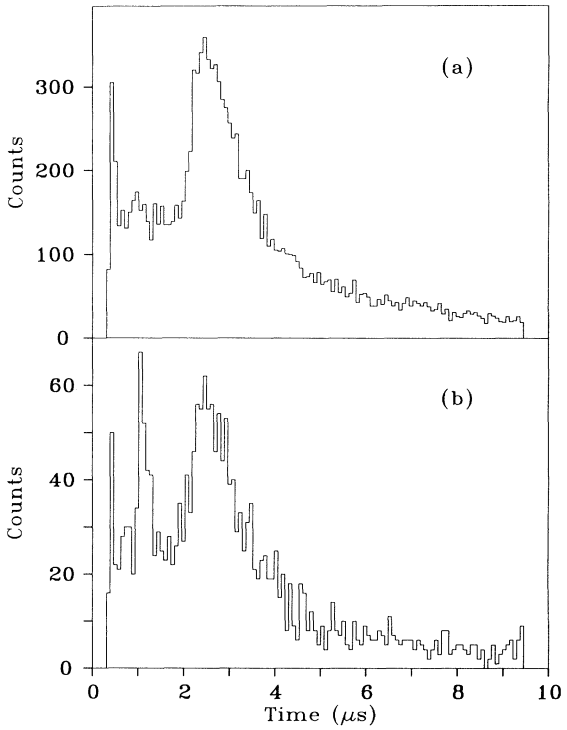

FIG. 14. Summed time spectra with (b) and without (a) high frequency disturbances caused by the laser.

by adjusting the spark gap. Data with such disturbances were not included in the final analysis.

E. Normalization of resonant counts

All measured parameters were used to constitute two independent groups of data:

(i) Energy $E_{\text{c.m.}}$ of the laser photons in the rest frame of the phosphorus ion [Eqs. (3.2)–(3.5)]. This energy depends on the laser wavelength in the laboratory system, the ion-beam energy, the energy loss in the stripper foil, and the laser-ion beam angle for the Doppler shift correction. All these values determine values along the ordinate of the Lorentzian resonance curve in Fig. 16.

(ii) Number of resonant counts N^{res} which determines values on the abscissa of the resonance curve.

The number of measured resonant events N^{res} is proportional to the laser pulse energy P and the ion-beam intensity, neglecting dead time effects. The beam intensity is proportional to the background counts $N(t^B)$ caused by the decay of the metastable $2s\,^2S_{1/2}$ state. Since P_{in} and $N_{in}^B = N(t_{in}^B)$ can vary for different measuring points i within a single measurement cycle n, it is necessary to normalize the number of counts N_{in}^{res}. For this we used Eq. (5.1):

$$\overline{N}_{in}^{\text{res}} = \frac{1}{N_{in}^B}\left(\frac{1}{7}\sum_{j=1}^{7} N_{jn}^B\right)\frac{1}{P_{in}}\left(\frac{1}{7}\sum_{j=1}^{7} P_{jn}\right) N_{in}^{\text{res}}. \quad (5.1)$$

The index i varies from 1 to 7 for the seven positions per cycle. Because the differences among N_{in}^B and P_{in} in one cycle are small, the sum factors in Eq. (5.1) lead to a ratio $\overline{N}_{in}^{\text{res}}/N_{in}^{\text{res}} \approx 1$, where $\overline{N}_{in}^{\text{res}}$ is the normalized number of resonant counts. Thus the normalized number has the same statistics as the unnormalized number of resonant counts. The error in the correction due to the number of ions is small because the background was measured with a large time window compared to the time window for resonant counts ($t^B/t^{\text{res}} \approx 1000$). Furthermore the ion-beam intensity was not correlated with the wavelength.

A much more delicate correction is due to the laser pulse energy. Because this variable parameter depends on the laser wavelength, one is able to reduce the effect of normalization by selecting an optimal ion-beam energy. Specifically, if the gain profile of the laser is symmetrical around the centroid of the resonance curve, the normalization affects only the width Γ and not the centroid E^0 of the curve.

There is another effect which results in a systematic error. The wavelength of the laser could be tuned only towards increasing wavelengths [48]. It follows that the *right* side of the resonance curve was always measured with a lower laser energy than the *left* side because the laser pulse energy decreased with the number of pulses.

The effects described above can result in an apparent shift of the resonance energy. The effect is caused only by the different dead times on both sides of the resonance curve. To verify that the effect of the dead time of the proportional counters is small, in Fig. 15 the number of resonant counts is plotted versus the laser pulse energy times the background counting rate which is proportional to the ion-beam intensity. No clear deviation from a straight line can be recognized. A detailed description of the dead time correction is given in [28,38]. Table VIII contains the uncertainties caused by the data normalization.

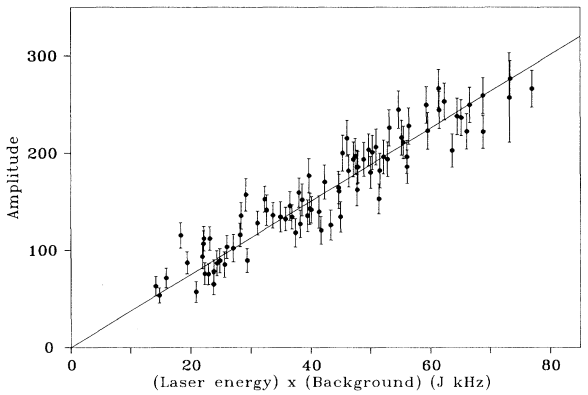

FIG. 15. Number of resonant counts vs laser energy times number of background counts. The good fit of the straight line indicates that there are no significant dead time effects.

TABLE VIII. Uncertainties caused by the data normalization.

Normalization	Relative	ΔE (meV)
Laser energy	$< 3 \times 10^{-3}$	0.027
Ion-beam intensity		0.001
Dead time		0.040

F. Resonance curve and error table

The normalized resonant counts $\overline{N}_{in}^{\text{res}}$ of each cycle n were fitted to a Lorentzian distribution by a χ^2 fit:

$$\overline{N}_{in}^{\text{res}} = N_n^0 \frac{\left(\frac{\Gamma_n}{2}\right)^2}{(E_{in} - E_n^0)^2 + \left(\frac{\Gamma_n}{2}\right)^2}. \tag{5.2}$$

The E_{in} are the $E_{\text{c.m.}}$ for each position i. One obtains from the fit to the seven points $(E_{1n}, \overline{N}_{1n}^{\text{res}}), \ldots, (E_{7n}, \overline{N}_{7n}^{\text{res}})$ the three parameters N_n^0, Γ_n, and E_n^0 for every cycle n. The fitted FWHM Γ_n of the resonance is very sensitive to distortions of the data from the Lorentzian shape. Weighted with their statistical significance, the centroids E_n^0 of all cycles were averaged to give the resulting centroid energy $\langle E^0 \rangle$ of the resonance.

Care has to be taken to give an error for $\langle E^0 \rangle$ of a single run and for the weighted average of all three runs. Only the statistical errors were combined quadratically. Any systematic error which leads to a shift of the Lorentzian curve or to a shape change of the resonance has to be added linearly to the overall error of the combined E^0. Fortunately most effects give a negligible error contribution, as for example the analytical form of the resonance or the asymmetry of the laser wavelength spectrum.

In Table IX the errors of all three measurements are given. The single error contributions (discussed in Tables VI–VIII) are split into independent groups, so that it is possible to combine the errors of various groups quadratically.

To show the consistence of the experimental data the 400 Lorentzian curves were normalized to the peak of the average, summed, and plotted in Fig. 16. The statistics are about 15000 counts in each of the three points near the maximum of the resonance. The error bars represent only the statistical errors due to resonant and background events. In the upper part of Fig. 16, the number of resonant events divided by the value of the fitted Lorentzian curve is plotted. This Lorentzian curve was not used to obtain the Lamb shift but only to show the statistics. For evaluating the Lamb shift, the Lorentzian curves were not normalized.

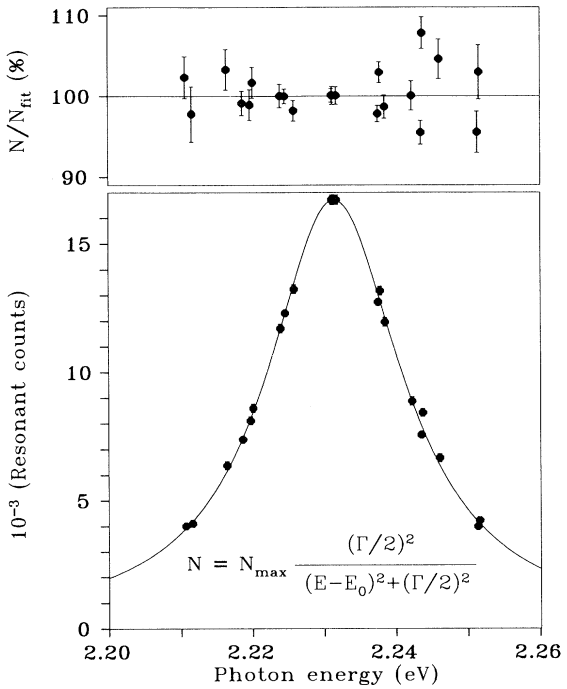

FIG. 16. Curve of resonant counts vs laser photon energy. The error bars represent only the statistical uncertainty including that of the background. The resonant peak was normalized to the average of the three measurements. These data were combined only to show the statistics and were not used for evaluating the Lamb shift.

TABLE IX. Error contributions in each of the three series of measurements.

	ΔE (meV)		
Source of error	I	II	III
Energy loss	0.079	0.082	0.042
Wavelength	0.096	0.097	0.042
Normalization	0.057	0.049	0.048
Ion-beam energy	0.069	0.064	0.053
Statistics	0.100	0.093	0.090
Others	0.058	0.058	0.058
Quadratic sum	0.192	0.186	0.142

G. Statistical investigations

The asymmetric deviations from the Lorentzian shape have to be treated carefully to get a reasonable error for $\langle E^0 \rangle$. Symmetric deviations from the shape have a larger influence on the fit parameters. The most important effect on the experimental curve is the damping caused by dead time of the proportional counters. This can be understood by the larger loss of events in the middle of the resonance and is increased by larger laser-pulse energy and ion-beam current. Other effects which lead to a changed line shape are the finite spectral FWHM of the laser and the Doppler broadening of the photon energy. To diminish the influence of these on the fitted centroid E_n^0, the wavelengths λ_{in} were chosen at and symmetrically around the supposed centroid. It is straightforward that for perfectly symmetrically points there is no error from this in the E_n^0 fit parameter. Only Γ_n and N_n^0 are affected. Analytical calculations show that small deviations from symmetry of the points around E_n^0 lead in first order to only an altered Γ_n. Fixing Γ_n causes a change in

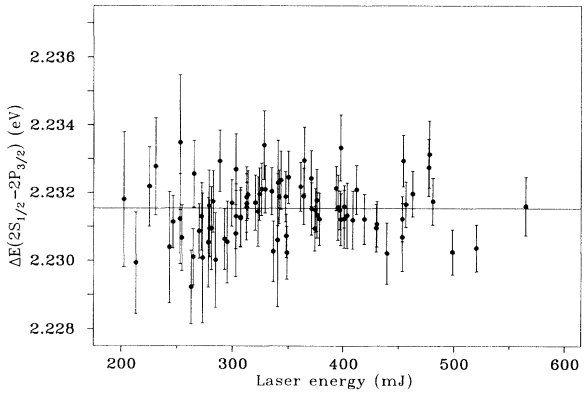

FIG. 17. Measured centroid energy of the $2s\,^2S_{1/2}$–$2p\,^2P_{3/2}$ transition vs the pulse energy of the laser. The fitted straight line shows that there is no dependence of measured transition energy and laser energy.

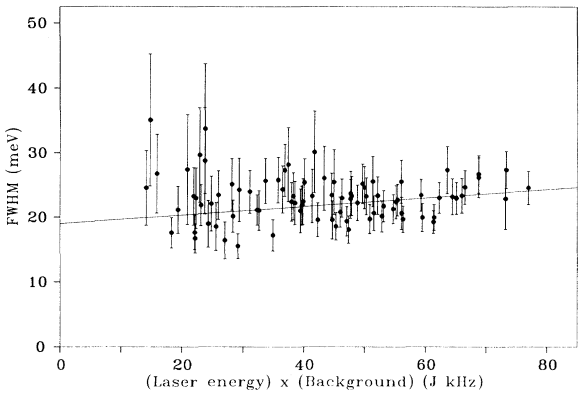

FIG. 19. FWHM of the Lorentzians for the third run vs the laser pulse energy times background counting rate. Extrapolating the fit data to the ordinate, one gets FWHM $\langle\Gamma\rangle = 18.4(10)$ meV.

N_n^0, but not in E_n^0. This shows the importance of having N_n^0 as a fit parameter.

As a second test for the independence of E^0 from the line shape of the resonance a fit was made with a Gaussian instead of a Lorentzian curve. The deviation in the centroids was negligible compared to the position uncertainties given.

Because of the large number of measured resonance curves several statistical investigations could be made. In Fig. 17 for example the dependence of the measured $2s\,^2S_{1/2}$–$2p\,^2P_{3/2}$ energy on the laser-pulse energy P is shown. One notes that there is no significant correlation. This figure shows typical fit error bars for the Lorentzian centroids. On the average, they are smaller for larger laser-pulse energy because of more counts.

Figure 18 compares the histogram of the fitted E_n^0 for the last run with a Gaussian distribution of same centroid and width. Good agreement is found. Thus it is allowed to average the centroids to obtain an average value $\langle E^0\rangle$ for the whole measurement.

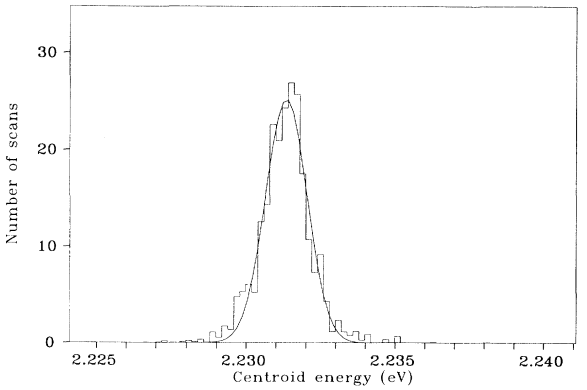

FIG. 18. Histogram of the measured centroids E_0^n. The distribution can be fitted to a Gaussian of the same FWHM. Therefore one can average the E_n^0 to obtain an $\langle E^0\rangle$ with a meaningful error.

The FWHM $\langle\Gamma\rangle$ of the resonance is obtained from the values Γ_n by extrapolation to zero laser-pulse energy and zero background. One expects the FWHM to be broadened with increasing laser power and ion-beam current. The straight line fitted to the data shown in Fig. 19 confirms this. The error bars in Fig. 19 are again the uncertainty of the fits. As before, one can see a decreasing error with increasing laser power and ion current due to statistics.

H. Results

Table X contains the experimental $2s\,^2S_{1/2}$–$2p\,^2P_{3/2}$ transition energies $\langle E^0\rangle$ as measured with contributing errors, the deduced Lamb shift $\langle E_{\rm LS}\rangle$ with its errors, and the experimental width $\langle\Gamma\rangle$ of all three measurements together with the theoretical values [17,18]. The Lamb shift was calculated with the theoretical value for the fine-structure splitting $E(2p\,^2P_{1/2} - 2p\,^2P_{3/2}) = 2.314\,82(2)$ eV given by [17,18]. The overall error is not much different from the individual measurements because some errors were systematically the same. Only the statistically independent errors were added quadratically.

I. Comparison with theory and other experiments

The $2s\,^2S_{1/2}$–$2p\,^2P_{1/2}$ energy splitting has been measured for several hydrogenlike species. Results having

TABLE X. Results of all three runs. Σ indicates the weighted average, $\langle E^0\rangle$ is the measured $2s\,^2S_{1/2}$–$2p\,^2P_{3/2}$ energy splitting.

	$\langle E^0\rangle$ (eV)	$\langle E_{\rm LS}\rangle$ (meV)	$\langle\Gamma\rangle$ (meV)
Theory		83.764(50)	20.9
Run I	2.23137(19)	83.45(19)	19.0(5)
Run II	2.23143(19)	83.39(19)	20.9(10)
Run III	2.23122(14)	83.60(14)	18.4(10)
Σ	2.23133(12)	83.49(12)	19.2(4)

small errors have been compiled in Ref. [49]. The theoretical values were taken from the calculations by Mohr [17] and Johnson and Soff [18] which both give the same values. Figure 20 shows this comparison of experimental values normalized to the theoretical predictions. The present value of the P^{14+} measurement falls 2.1 standard deviations below the theory. Most of the other experimental values in the region of $Z \leq 18$ determined by various methods show the same tendency, but the deviations are not statistically significant.

J. Higher order test in $(Z\alpha)$

As discussed in Sec. II the self-energy gives the dominant contribution to the Lamb shift. The uncertainty in calculating the self-energy with Eq. (2.1) arises mainly from the theoretical function $G(Z\alpha)$. Using the theoretical contributions not belonging to the self-energy and the experimental data one can define a new function $\tilde{G}(Z\alpha)$. Assuming all other terms in Eqs. (2.6) and (2.1) to be correct, $\tilde{G}(Z\alpha)$ and $G(Z\alpha)$ should be identical. The energies in Eq. (5.3) are the experimental E_{expt} and the theoretical E_{theor} values of the Lamb shift:

$$\tilde{G}(Z\alpha) = G(Z\alpha) + \frac{6\pi}{\alpha(Z\alpha)^6 mc^2}\,[E_{\text{expt}} - E_{\text{theor}}]\,. \quad (5.3)$$

$\tilde{G}(Z\alpha)$ includes the experimental uncertainties as well as the theoretical ones. This function allows a comparison of different experiments in testing the significance of higher orders in $(Z\alpha)$ included in $G(Z\alpha)$. In Fig. 21 the quantity $\tilde{G}(Z\alpha)/G(Z\alpha)$ is plotted. Although the experimental values for hydrogen have the smallest uncertainties, the test significance for higher order terms in $(Z\alpha)$ for phosphorus or sulfur is much better. This can be understood by the Z^2 scaling of $G(Z\alpha)$ relative to the Lamb-shift values and the theoretical uncertainties included in Eq. (5.3). Taking into consideration the negative values of $G(Z\alpha)$, one can recognize the same tendency of all experimental data for $Z > 9$ towards lower $2S$ Lamb-shift values which was already suggested in Fig. 20.

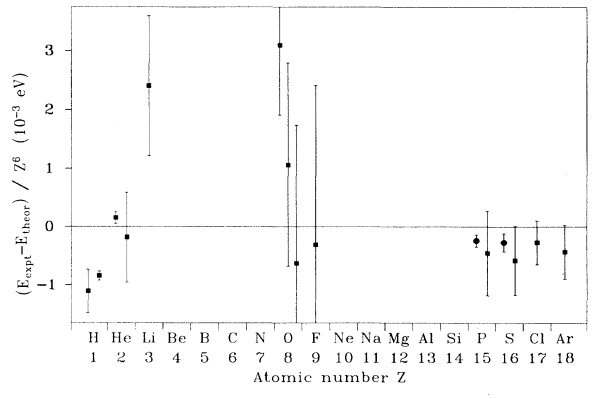

FIG. 20. Experimental values of the Lamb shift compared to theoretical predictions. ● indicates the two measurements (P,S) done by the present group. The respective references for the other measurements (■) from H to Ar are [50]–[62].

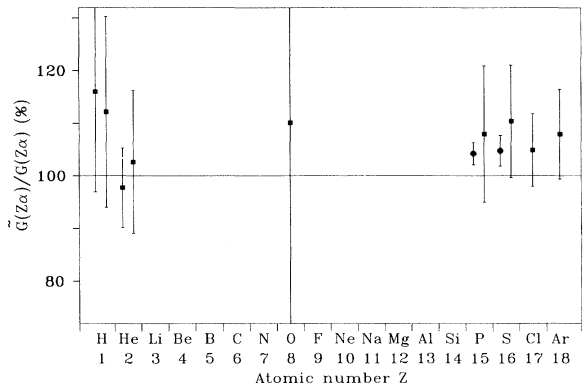

FIG. 21. Experimental values of $\tilde{G}(Z\alpha)$ in percentage of the theoretical predictions $G(Z\alpha)$. ● indicates the two measurements made by the present group. The respective references for the other measurements (■) from H to Ar are [50]–[53], [57], [59]–[62]. The data of Fig. 20 not included in this figure have too large uncertainties to be depicted.

VI. FUTURE PERSPECTIVES

The experimental values for the Lamb shift have a tendency to be lower than the theoretical predictions, but there is not yet statistical significance to this behavior. More accurate experiments are clearly necessary. A good possibility to decrease the experimental uncertainty is the newly proposed auto collimation spectroscopy for fast hydrogen ions described in Ref. [63]. This method uses a pulsed bidirectional laser beam having a fixed wavelength in connection with a high current pulsed ion beam [64]. Depending on the angle to the ion beam, monoenergetic laser photons in the laboratory system E_{lab} have two different energies E_F and E_R in the rest frame of the ions. For a suitable wavelength two points on opposite sides of the resonance can be measured simultaneously. If $N(E_F)$ is made equal to $N(E_R)$ by varying the ion velocity β, the resonance energy E^0 is determined by

$$E^0 = \frac{E_F + E_R}{2} = \frac{E_{\text{lab}}}{\sqrt{1-\beta^2}}. \quad (6.1)$$

The main advantages of this method are as follows:

(i) Only a single wavelength is necessary to determine the resonance energy. This provides an accurate measurement of both the wavelength and the laser pulse energy.

(ii) The $\beta\cos(\theta)$ term in the Doppler shift Eq. (3.2) cancels, thus the precision necessary in the determination of β is decreased by one order of magnitude.

(iii) The absolute value of the angle θ does not enter into the resonance energy E^0; it determines solely the difference $E_F - E_R$. Changing the angle θ the resonance curve can be scanned.

ACKNOWLEDGMENTS

We wish to thank a certain number of persons who made important contributions in the course of these Lamb-shift experiments: L. Degener, J. D. Fox, A. P. Georgiadis, L. von Gerdtell, C. F. Moore, U. Scharfer, and H. D. Sträter, who participated in the initial stage of these measurements; Professor Dr. G. Soff for reading parts of this paper and for useful discussions; the staff of the MP tandem accelerator in Strasbourg and in particular the data acquisition group; on the part of the Institut für Kernphysik researchers, the kind hospitality of the CRNS in Strasbourg; the mechanical and electronics services at the Institute in Köln, and in particular L. Fruh and L. Przybylski for building many superb devices. We acknowledge the support of the Deutsche Forschungsgemeinschaft for this experiment under Contract No. Br799/2-4 and we further thank the Gesellschaft für Schwerionenforschung in Darmstadt for supporting an initial stage of this experiment.

[1] T. Kinoshita, in *The Hydrogen Atom*, edited by G. F. Bassani, M. Inguscio, and T. W. Hänsch (Springer-Verlag, Berlin, 1989), p. 247.
[2] G. T. Bodwin and D. R. Yennie, Phys. Rev. D **37**, 498 (1988).
[3] W. E. Lamb, Jr. and R. C. Retherford, Phys. Rev. **72**, 241 (1947).
[4] S. R. Lundeen and F. M. Pipkin, Meterologia **22**, 9 (1986).
[5] V. G. Pal'chikov, Yu. L. Sokolov, and V. P. Yakovlev, Lett. J. Tech. Phys. **38**, 347 (1983).
[6] L. N. Hand, D. J. Miller, and R. Wilson, Rev. Mod. Phys. **35**, 335 (1963).
[7] H. Grotch, Phys. Scr. **T21**, 86 (1988).
[8] G. G. Simson, Ch. Schmitt, F. Borkowski, and V. H. Walther, Nucl. Phys. A **333**, 381 (1981).
[9] G. C. Bhatt and H. Grotch, Ann. Phys. **178**, 1 (1987).
[10] J. Gassen, D. Müller, D. Budelsky, L. Kremer, H.-J. Pross, F. Scheuer, P. von Brentano, A. Pape, and J. C. Sens, Phys. Lett. A **147**, 385 (1990).
[11] D. Müller, J. Gassen, L. Kremer, H. J. Pross, F. Scheuer, H.-D. Sträter, P. von Brentano, A. Pape, and J. C. Sens, Europhys. Lett. **5**, 503 (1988).
[12] D. Müller, J. Gassen, D. Budelsky, L. Kremer, H.-J. Pross, F. Scheuer, P. von Brentano, J. C. Sens, and A. Pape, in *Laser Spectroscopy IX*, edited by M. S. Feld, J. E. Thomas, and A. Mooradian (Academic Press, San Diego, 1989).
[13] D. Müller, J. Gassen, F. Scheuer, L . Kremer, H.-J. Pross, D. Budelsky, P. von Brentano, J. C. Sens, and A. Pape, in *Atomic Physics 11*, edited by S. Haroche, J. C. Gay, and G. Grynberg (World Scientific, Singapore, 1989).
[14] A. Georgiadis, D. Müller, H.-D. Sträter, J. Gassen, P. von Brentano, J. C. Sens, and A. Pape, Phys. Lett. A **115**, 108 (1986).
[15] H.-D. Sträter, L. von Gerdtell, A. Georgiadis, D. Müller, P. von Brentano, J. C. Sens, and A. Pape, Phys. Rev. A **29**, 1596 (1984).
[16] A. van Wijngaarden, J. Patel, and G. W. F. Drake, in *Atomic Physics 11*, edited by S. Haroche, J. C. Gay, and G. Grynberg (World Scientific, Singapore, 1989), p. 355.
[17] P. J. Mohr, At. Data Nucl. Data Tables **29**, 453 (1983).
[18] W. R. Johnson and G. Soff, At. Data Nucl. Data Tables **33**, 405 (1985).
[19] G. W. Erickson, J. Phys. Chem. Ref. Data **6** (3), 831 (1977).
[20] G. Soff, P. Schlüter, B. Müller, and W. Greiner, Phys. Rev. Lett. **48**, 1465 (1982); G. Soff (private communication).
[21] E. H. Wichmann and N. M. Kroll, Phys. Rev. **101**, 843 (1956).
[22] G. Soff and P. J. Mohr, Phys. Rev. A **38**, 5066 (1988).
[23] P. J. Mohr, in *Beam-Foil Spectroscopy*, edited by I. A. Sellin and D. J. Pegg (Plenum, New York, 1976), p. 89.
[24] P. J. Mohr, Nucl. Instrum. Methods B **10**, 26 (1985).
[25] T. Beier and G. Soff, Z. Phys. D **8**, 129 (1988).
[26] G. W. Erickson and H. Grotch, Phys. Rev. Lett. **60**, 2611 (1988).
[27] G. C. Bhatt (private communication).
[28] D. Müller, Ph.D. Thesis, Institut für Kerphysik, Köln (1988).
[29] F. A. Parpia and W. R. Johnson, Phys. Rev. A **26**, 1142 (1982).
[30] R. Marrus, Nucl. Instrum. Methods **110**, 333 (1973).
[31] P. H. Heckmann and E. Träbert, *Einführung in die Spektroskopie der Atomhülle* (Vieweg Verlag, Braunschweig, 1980); R. Herdan and T. P. Hughes, Astrophys. J. **133**, 294 (1961).
[32] K. Omidvar, At. Data Nucl. Data Tables **28**, 1 (1983).
[33] U. Scharfer, C. Heinrichs, J. D. Fox, P. von Brentano, L. Degener, J. C. Sens, and A. Pape, Nucl. Instrum. Methods **146**, 573 (1977).
[34] J. Gassen, D. Müller, P. von Brentano, and A. P. Georgiadis, Opt. Commun. **76**, 131 (1990).
[35] H. O. Meyer, W. G. Weitkamp, J. S. Dunham, T. A. Trainor, and M. P. Baker, Nucl. Phys. A **269**, 269 (1976).
[36] G. M. Temmer, B. Teitelmann, R. van Bree, and H. Ogata, in *Proceedings of the International Conference on Nuclear Structure, Tokyo, 1967*, edited by S. Sanada (Journal of the Physical Society of Japan, Tokyo, 1968), p. 318.
[37] E. Huenges, H. Vonach, and J. Labetzki, Nucl. Instrum. Methods **121**, 307 (1974).
[38] J. Gassen, Ph.D. thesis, Institut für Kerphysik, Köln (1988).
[39] H.-D. Sträter, Ph.D. thesis, Institut für Kernphysik, Köln (1984).
[40] GCA/McPherson Instrument Acton Massachusetts Data Sheet, Scanning monochromator EU-700 and EUE-700 series (1968).
[41] F. Scheuer, Diploma thesis, Institut für Kernphysik, Köln (1989).
[42] Fairchild Camera and Instrument Corp. Data Sheet, CCD 133/143 (1979).
[43] Polytec Laser Precision Corp. Instruction Manual, Rj-7000 Series Radiometer, RjP-700 Series Probe (1984).
[44] Siemens Data Sheet, Durchflußzählrohr Typ F (1973).
[45] *Handbook of Chemistry and Physics*, edited by R. C. Weast, 52nd ed. (Chemical Rubber, Cleveland, 1971), p. E204.

[46] Ch. DeWitt Coleman, W. R. Bozman, and W. F. Meggers, *Table of Wavenumbers*, United States Department of Commerce, National Bureau of Standards Monograph No. 3 (U.S. GPO, Washington, DC, 1960), Vol. I, p. vi.
[47] Instrument Technology LTD Operating Instructions, Sub-Nanosecond Photodiode FD 125 High Current Fast Vacuum Photodiode (1986).
[48] A. Georgiadis, Ph.D. thesis, Institut für Kernphysik, Köln (1985).
[49] P. von Brentano, D. Müller, and J. Gassen, in *Conference on Spectroscopy and Collisions of Few Electron Ions, Bucharest, 1988*, edited by M. Ivascu, V. Florescu, and V. Zoran (World Scientific, Singapore, 1989).
[50] S. R. Lundeen and F. M. Pipkin, Phys. Rev. Lett. **46**, 232 (1981).
[51] V. G. Pal'chikov, Yu. L. Sokolov, and V. P. Yakovlev, Pis'ma Zh. Eksp. Teor. Fiz. **38**, 347 (1983) [JETP Lett. **38**, 418 (1983)].
[52] A. van Wijngaarden, J. Kwela, and G. W. F. Drake, Phys. Rev. A **43**, 3325 (1991).
[53] M. S. Dewey and R. W. Dunford, Phys. Rev. Lett **60**, 2014 (1988).
[54] M. Leventhal, Phys. Rev. A **11**, 427 (1975).
[55] G. P. Lawrence, C. Y. Fan, and S. Bashkin, Phys. Rev. Lett. **28**, 1612 (1972).
[56] M. Leventhal, D. E. Murnick, and H. W. Kugel, Phys. Rev. Lett. **28**, 1609 (1972).
[57] B. Curnutte, C. L. Cocke, and R. D. Dubois, Nucl. Instrum. Methods **202**, 119 (1982).
[58] H. W. Kugel, M. Leventhal, D. E. Murnick, C. K. N. Patel, and O. R. Wood II, Phys. Rev. Lett. **35**, 647 (1975).
[59] P. Pellegrin, Y. El Masri, and L. Palffy, Phys. Rev. A **31**, 5 (1985).
[60] V. Zacek, H. Bohn, H. Brum, T. Faestermann, F. v. Feilitzsch, G. Giorginis, P. Kienle, and S. Schuhbeck, Z. Phys. A **318**, 7 (1984).
[61] O. R. Wood II, C. K. N. Patel, D. E. Murnick, E. T. Nelson, M. Leventhal, H. W. Kugel, and Y. Niv, Phys. Rev. Lett. **48**, 398 (1982).
[62] H. Gould and R. Marrus, Phys. Rev. A **28**, 2001 (1983).
[63] D. Müller, J. Gassen, F. Scheuer, H. D. Sträter, and P. von Brentano, Z. Phys. D **18**, 249 (1991).
[64] D. Platte, Diploma thesis, Institut für Kernphysik, Köln (1990).